Modeling and experimental verification of a tubular actuator for 20-g acceleration in a Pick-and-Place Application

Modeling and Experimental Verification of a Tubular Actuator for 20-g Acceleration in a Pick-and-Place Application

Koen J. Meessen, *Student Member, IEEE*, Johannes J. H. Paulides, *Member, IEEE*, and Elena A. Lomonova, *Senior Member, IEEE*

***Abstract*—This paper presents the modeling and the experimental verification of a tubular actuator for a pick-and-place application. To increase the throughput of a placement robot for printed circuit boards, a very fast linear motion is required. A moving-magnet tubular actuator with axially magnetized magnets is selected. Using a semianalytical magnetic field model coupled to a thermal one, a design is created that achieves a translator acceleration of 20 g. A prototype of the designed actuator is built and coupled with a Simulink dSpace system to perform extensive measurements in order to validate the models and investigate the achievable acceleration within a predetermined motion profile. The electromotive force is measured, and the disturbance forces are identified. The position error is measured during the motion profile with an acceleration of 20 g and a stroke of 30 mm. Furthermore, thermal measurements are performed to check the achievable duty cycle. The built design shows good agreement with the models, and the specified acceleration of 20 g is achieved.**

***Index Terms*—High acceleration, linear actuator, measurements, permanent magnet.**

I. Introduction

In ROBOTIC applications, there is an increasing demand for fast actuation with high precision and bandwidth capabilities. One particular application is the pick-and-place (P&P) robot that places surface-mounted devices on printed circuit boards, which are picked from a feeder. The complete P&P action requires a four-degree-of-freedom robotic motion; however, this paper focuses on the linear motion in the vertical direction to pick and place the components. To increase the throughput of the total P&P cycle, currently reaching a maximum of 8000 components/h, a high acceleration level is necessary. The aim of this paper is to design an actuator with a very high translator acceleration of 200 ms^{-2} on a stroke of 30 mm for a duty cycle of 30%. As can be seen in Fig. 1, the motion profile consists of an acceleration phase, resulting in a velocity of 1.5 ms^{-1}, which is followed by a deceleration phase to be able to standstill in the upward position at $z = 30$ mm.

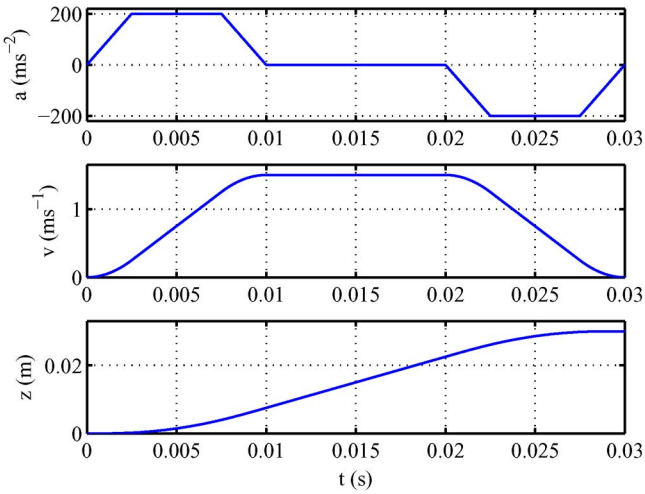

Fig. 1. Motion profile with a peak acceleration of 200 ms^{-2}, a peak velocity of 1.5 ms^{-1}, and a stroke of 30 mm.

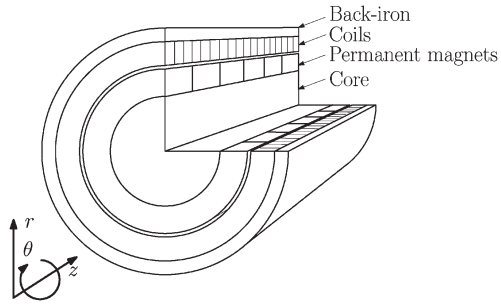

Fig. 2. Moving-magnet slotless tubular permanent-magnet actuator.

To achieve this motion profile, a three-phase slotless tubular permanent-magnet actuator is selected, as shown in Fig. 2, since it has a high force density and very good servo characteristics [1]. The tubular actuator consists of a stator and a translator, where a moving-magnet concept is preferred, since it does not require winding connections to the moving part. Furthermore, the stator contains coils and is chosen to be slotless as the actuator is designed for a precision positioning application, which requires a smooth force characteristic. An additional advantage is the manufacturability of a slotless structure, particularly in

Manuscript received July 9, 2009; revised October 15, 2009 and January 4, 2010; accepted February 11, 2010. Date of publication July 12, 2010; date of current version September 17, 2010. Paper 2009-EMC-235.R2, presented at the 2009 IEEE International Electric Machines and Drives Conference, Miami, FL, May 3–6, and approved for publication in the IEEE Transactions on Industry Applications by the Electric Machines Committee of the IEEE Industry Applications Society.

The authors are with the Eindhoven University of Technology, 5600MB Eindhoven, The Netherlands (e-mail: k.j.meessen@tue.nl; j.j.h.paulides@tue.nl).

Color versions of one or more of the figures in this paper are available online at http://ieeexplore.ieee.org.

Digital Object Identifier 10.1109/TIA.2010.2057392

low volume actuators, since the stator consists solely of a soft-magnetic tube.

As the application of this actuator is a P&P machine to place very small components on printed circuit boards, the load of the actuator is negligible compared to the force required to accelerate the translator and, hence, is not taken into account.

II. Modeling

To model the actuator, a multiphysical model is created where magnetic and thermal models are coupled resulting in a very fast accurate analysis and design tool. The magnetic properties are described using a semianalytical description of the magnetic fields.

A. Magnetic Model

Several papers have been written on the subject of designing the tubular actuators using semianalytical field equations. In [2]–[4], semianalytical solutions for the magnetic fields in different tubular-actuator topologies are presented, and [5] compares the force density of three different topologies. Although these papers are very extensive, the conclusions from [5] cannot be used in this paper as the force is maximized instead of the acceleration. These two quantities are strongly connected but show different optima. Therefore, the semianalytical model described in [2]–[4] is used to design an actuator for a high translator acceleration.

In this model, the magnetic field due to the permanent magnets is described while the coils are modeled as air. Hence, the armature reaction field is not considered in the model, and the force is calculated using the Lorentz force equation. The formulation for the magnetic field is obtained by solving the magnetostatic field equations using the magnetic vector potential $\vec{A}$ defined as

$$\vec{B} = \nabla \times \vec{A} \tag{1}$$

where $\vec{B}$ is the magnetic flux density. Due to the symmetry in the circumferential direction in the tubular actuators, the magnetic flux density$\vec{B}$ has only an r- and a z-component. Therefore, the magnetic vector potential has only a circumferential θ-component. In the model, the following assumptions are made.

1) The soft-magnetic parts are infinitely permeable.
2) The actuator is infinitely long, and the end effects are later calculated using finite-element modeling.
3) The permanent magnets have a linear demagnetization characteristic and are fully magnetized in the direction of magnetization.

Different regions have to be considered where, in the source free regions (translator core, air gap, and coils), the Laplace equation has been solved

$$\nabla^2 \vec{A} = 0 \tag{2}$$

and, in the permanent magnet regions, the Poisson equation has been solved

$$\nabla^2 \vec{A} = -\mu_0 \nabla \times \vec{M} \tag{3}$$

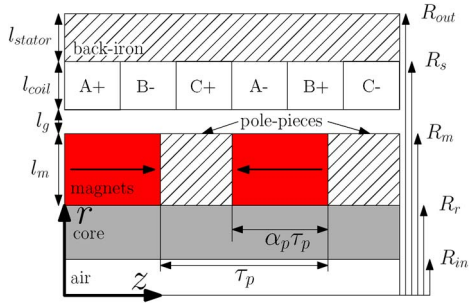

Fig. 3. One pole pair of an axially magnetized slotless tubular actuator.

where $\vec{M}$ is the magnetization vector describing the magnet array on the translator by a Fourier series. The solution for $\vec{B}$ is obtained by applying boundary conditions on the interfaces of the regions. The magnetization and, hence, the flux density equations are Fourier series containing an infinite sum. As the implemented model is an approximation over a finite number of harmonics, the model is not fully analytical.

B. Electrical Model

As the slotless actuators exhibit no cogging force due to stator slotting and because the flux density in the coil contains a negligible amount of higher harmonics, there is no need for a winding configuration that aims to reduce electromotive force (EMF) harmonics or cogging forces. To obtain a high winding factor, full-pitch brushless ac windings with a coil pitch equal to the pole pitch are implemented, as shown in Fig. 3. As a current amplifier with an output filter is used to drive the actuator, there is no need for a specific inductance value to filter the higher harmonics in the current. Therefore, the inductance value is not taken into account in the model.

While the magnetic fields are primarily limited by material properties, the electrical properties of the actuator are mainly restricted by thermal constraints. Naturally, the current density in the coil region results in a copper loss which defines the heat produced in the windings where the copper loss per meter stator is equal to

$$P_{\mathrm{Cu}} = \frac{J^2}{k_{\mathrm{p}}} l_{\mathrm{coil}} \rho_{\mathrm{Cu}} 2\pi \left(R_s - \frac{l_{\mathrm{coil}}}{2} \right) \tag{4}$$

where J is the rms current density in the coil and k_{p} is the packing factor of the coil region. Additionally, eddy-current losses produce heat in the back iron. Due to these two heat sources, the temperature difference between the armature and the ambient rises to

$$\Delta T = \frac{P_{\mathrm{Cu}} + P_{\mathrm{eddy}}}{2\pi R_{\mathrm{out}} h} \tag{5}$$

where h is the convection coefficient and P_{eddy} is the eddy-current losses in the back iron per meter stator. In (4) and (5), the following assumptions are made.

1) The coil and back iron are assumed to be perfect heat conductors which is a good approximation [6].
2) The only heat flow is through the back iron, and the heat flow through the stator ends and translator is neglected.

3) The convection coefficient is independent of the temperature.

The convection coefficient can have values of approximately 20 $\mathrm{Wm^{-2}K^{-1}}$ for natural cooling and up to 70 $\mathrm{Wm^{-2}K^{-1}}$ when forced air cooling is used [7].

C. Force and Acceleration

As the considered actuator has no slots, the thrust force can be calculated by applying the Lorentz force equation (6) in the coil region

$$\vec{F}_z = \int_{V_{\mathrm{coil}}} (\vec{J} \times \vec{B})\, dV. \tag{6}$$

The total force on the translator in the axial direction is

$$\vec{F}_{\mathrm{tot}} = \vec{F}_z + \vec{F}_{\mathrm{d}} \tag{7}$$

where $\vec{F}_{\mathrm{d}}$ is the distortion force caused by the end-effect cogging and friction. The translator acceleration is defined by the produced force due to the current in the coils $\vec{F}_z$ divided by the total translator mass which depends on the stroke and the active length. Hence, the distortion force is not taken into account during the optimization of the acceleration as this component has a zero mean value and will be minimized in a later stage using a finite-element model.

III. Design

The models presented in the previous sections are coupled to create a multiphysical design tool. Using this tool, a parametric search is performed to find the geometric parameters which provide the highest translator acceleration for a value of $\Delta T = 40\ ^{\circ}\mathrm{C}$. In the parametric search, the eddy-current losses are not taken into account in calculating ΔT.

An axially magnetized topology, as shown in Fig. 3, is chosen because this topology contains less permanent-magnet material than, for example, a Halbach topology, and all magnets are magnetized in the (easy magnetizable) axial direction. The translator core is made of aluminum to minimize the translator mass.

Because of the constraints of the actuator application, the length of the back iron L_{bi} of the actuator has an upper bound of 105 mm, and the outer radius R_{out}, inner radius R_{in}, and air-gap length l_g are fixed in the parametric sweep. As the components in the application are attached to the translator using vacuum, a hollow core is required; therefore, $R_{\mathrm{r}} \geq 2.0$ mm and $R_{\mathrm{in}} = 1.0$ mm. The values for these fixed parameters can be found in Table I as well as the values of the other parameters of the final design.

The design is obtained from a parametric search, as shown in Fig. 4. The geometric parameters are varied between the predefined minimum and maximum values. Using the constrained ΔT, the copper loss is calculated using (5). Consequently, the maximum current density is calculated using (4) resulting in an rms value for the current density that can be applied to the windings continuously without exceeding the maximum temperature. A duty cycle is calculated to represent the fact that the current follows the acceleration waveform shown in Fig. 1, and because the translator is at standstill at $z = 0$ and $z = 30$. Dividing the rms value of the current density by this duty cycle, the peak value of the current density and, consequently, the peak value of the force are calculated. Using the mass of the translator, the peak acceleration is calculated. This acceleration level is now mainly limited by the achievable convection coefficient and the temperature constraint. The convection coefficient is fixed to 20 $\mathrm{Wm^{-2}K^{-1}}$.

Since the analytical model used in the parametric search assumes infinitely permeable iron, saturation is not taken into account in the model. To check this assumption, the magnetic flux density is calculated in the iron parts, i.e., pole pieces and stator back iron, of the actuator, as shown in the flow chart in Fig. 4. The flux (obtained from the semianalytical model) entering the iron parts is divided by the smallest cross section of the flux path resulting in a peak flux density. A predefined upper limit of the flux density without having highly saturated iron, 1.7 T, is compared with the peak flux density calculated in the design cycle. If the latter value exceeds the limit of 1.7 T, the result of the force calculation is assumed to be unreliable and is not saved.

Consequently, another geometric parameter is changed, and the same procedure is repeated until all parameters have been changed between their minimum and maximum values. When

TABLE I
GEOMETRIC PARAMETERS PROTOTYPE

Geometric parameter		Description
R_{out} (mm)	9.25	Outer radius
l_{stator} (mm)	1.00	Radial stator length
l_{coil} (mm)	2.00	Radial coil length
l_g (mm)	0.25	Radial airgap length
l_m (mm)	4.00	Radial magnet length
τ_p (mm)	8.33	Pole pitch
α_p	0.75	magnet pitch to pole pitch ratio
L_{bi} (mm)	100	Stator back-iron length
N_{coils}	36	Number of coils
N_{pp}	8.5	Number of pole pairs on translator
N_{ppa}	6	Number of active pole pairs
L_{ax} (mm)	143.7	Total translator length
$m_{translator}$ (g)	151	Translator mass

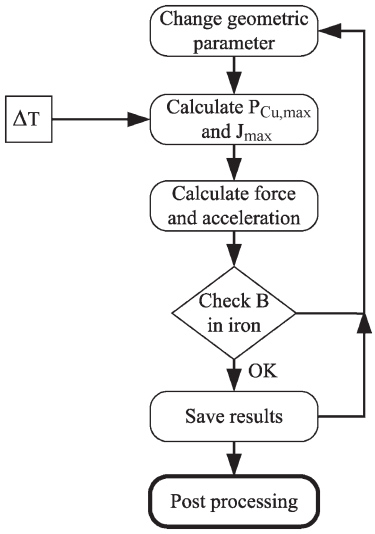

Fig. 4. Flowchart of the design cycle.

TABLE II
MATERIAL PROPERTIES PROTOTYPE

Property	Value	Description
Magnet	BM35H	Permanent magnet material
B_{rem} (T)	1.175	Remanent flux density permanent magnet
μ_r	1.08	Relative permeability permanent magnet
Steel	AI1010	Steel type
ρ_{Cu}	$1.7\text{x}10^{-8}$	resistivity of copper
k_p	0.6	Coil packing factor

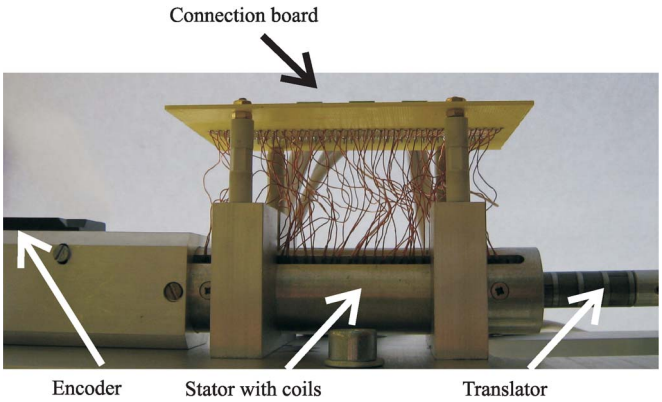

Fig. 5. Prototype of the designed slotless permanent-magnet tubular actuator.

all the calculations are finished, the results are postprocessed. All the results are graphically represented and compared to obtain the actuator with the highest acceleration.

A finite-element model of the final design with the dimensions from Table I and the material properties from Table II is made to calculate the eddy-current losses during the motion profile shown in Fig. 1. The results show that the eddy-current losses are only 4% of the total losses and, hence, the assumption during the design procedure to neglect the eddy-current losses is a valid approximation.

IV. SETUP

The design presented in the previous section is built as shown in Fig. 5. At the left side of the picture, the optical position encoder (Renishaw RGH22) is visible. The actuator contains 36 coils which are all separately soldered to a 36-pin connector on the connection board. This provides the possibility to create different winding and phase configurations using a second printed circuit board. For the results presented in this paper, the coils of the three phases are connected in series while all the three phases are separately driven by a current controller and, hence, not wye or delta connected. The coils and the back iron are encased by an aluminum tube to enable the fixation of the bearings. Two nylon sliding bearings are used at both end of the armature. As can be seen, a slit is milled in the aluminum tube and the back iron to provide a feedthrough for the windings of the coils to the connection board. The width of the slit in the back iron is 1.0 mm, which is less than 2% of the total back-iron material.

A 3-D finite-element analysis is performed to investigate the influence of the slit on the magnetic loading. To simplify the model, only one pole pitch is modeled, and the symmetry in the axial direction is used. In Fig. 6, the flux density in the radial direction near the back iron at $r = 8.20$ mm is shown

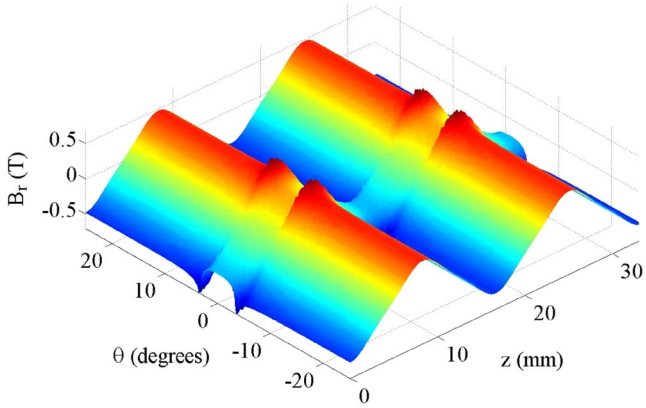

Fig. 6. Radial flux density near the slit at $r = 8.20$ mm.

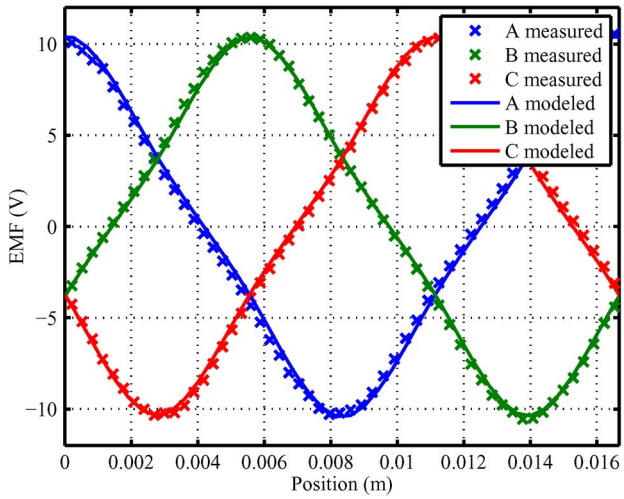

Fig. 7. Electromotive force at a speed of 1 m/s, both the measured and the modeled waveform.

for an angle of 25° to both sides with respect to the center of the slit. As can be seen, close to the edges of the slit, the curve shows a peak while, in the middle of the slit, the flux density is decreased. The flux in the center of the coil is integrated over the whole circumference and is compared to the solution obtained for a model without the slit. The difference in the flux density in both models is 0.11% in the center of the air gap and 0.15% close to the back iron. Consequently, the slit results in a negligible decrease of the magnetic loading. An advantage of the slit is the cut in the path of the eddy currents created by the movement of the translator and the armature reaction. To verify the analysis tool and to check the design specifications, several static and dynamic tests are performed.

V. ELECTROMOTIVE FORCE

Two magnets are characterized to obtain the correct remanent flux density and relative permeability. The measurements show that the remanent flux density is slightly lower than the value used in the modeling, i.e., 1.11 T instead of 1.175 T. The models are updated with the measured remanent flux density to be able to make a good comparison.

The EMF is measured by moving the translator with a certain speed through the actuator. In Fig. 7, the EMF of the three

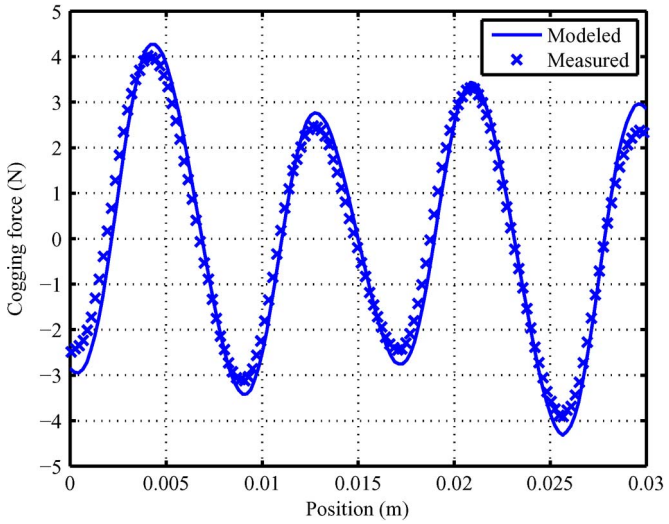

Fig. 8. Cogging force due to finite back iron and translator length for a back-iron length $L_{\rm bi} = 100.0$ mm, modeled by a finite-element model and measured on the prototype. $z = 0.015$ is the center position of the translator, as shown in Fig. 9.

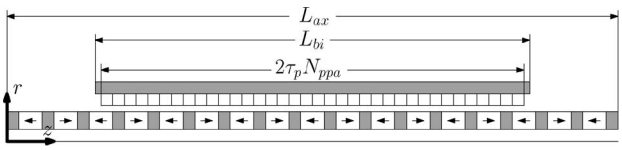

Fig. 9. Tubular actuator with the translator in its center position ($z = 15.0$ mm).

phases is shown, where the solid line shows the modeled EMF and the marks represent the measured values. As can be seen, the measurements are not exactly in phase with the model which can be caused by several effects. For example, the magnets might be not identically magnetized, the pole pitch varies, or the coil pitch varies. Although the results show good agreement with the model, the small deviation directly affects the performance by means of a smaller motor constant and a possible position error.

Fig. 7 shows that, in addition to the first harmonic, the third harmonic is present in the EMF. Because each single phase is connected to the amplifier and not wye connected, the third harmonic is not canceled in the EMF; hence, this third harmonic is apparent in the current as well.

VI. End-Effect Cogging Force

Although the actuator is slotless and, consequently, has no slot cogging, the finite stator length results in a cogging-force component which can be significant. Due to the abrupt change in the permeance of the magnetic path at the stator back-iron ends, attraction forces in the axial direction occur. Varying only the axial length of the back iron is one of the methods that can be used to minimize this force [8]. The prototype back iron has an axial length of a multiple of the pole pitch, which results in an end-effect cogging force of up to 15% of the rated force. Fig. 8 shows the measured end-effect cogging compared to the results from the models.

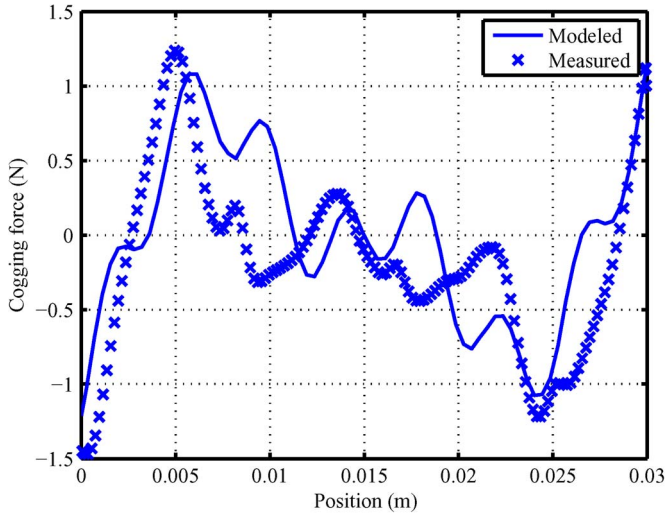

Fig. 10. Cogging force due to finite back iron and translator length for a back-iron length $L_{\rm bi} = 104.2$ mm, modeled by a finite-element model and measured on the prototype. $z = 0.015$ is the center position of the translator, as shown in Fig. 9.

A. Measurements of End-Effect Cogging Force

Two methods are used to measure the end-effect cogging force. First, a load cell is placed between the translator and the fixed world. Using a setscrew, the translator is moved to the left and to the right. The obtained waveform contains information about the end-effect cogging force and the friction. The offset between moving to the left or the right is equal to twice the friction. A disadvantage of this method is that the load cell has to be aligned very accurately for a reliable measurement, and additional equipment is required. The second method is based on a measurement of the current required to compensate the end-effect cogging forces. A controller is implemented with a high integrator gain resulting in a small position error. A trajectory with a constant velocity results in a constant friction; hence, the resulting current contains a constant-friction component and the end-effect cogging. Note that, here, the assumption is made that the friction is not position dependent. The two methods show good agreement, and the latter one is used in Fig. 8. As can be seen, the waveform of the measurement and the simulation model are in good agreement.

B. Minimization of End-Effect Cogging Force

Initially, the cogging force is measured and compensated by using a feedforward control at the cost of additional losses due to the increased current. Therefore, the back iron is adapted to decrease this force component. As mentioned before, the end-effect cogging force is a function of the axial length of the translator and, hence, can be minimized by choosing a proper length. An additional finite-element model is created to find the optimal length. A soft-magnetic ring is manufactured with the correct axial length and fixed inside the bearing directly onto the back iron. Although the ring and the back iron are not in contact over the whole circumference, from a magnetic point of view, the space between the two is negligible as the effective air gap between the back iron and the magnets is significantly larger.

A new end-effect cogging force measurement is undertaken to validate the improvement. The results in Fig. 10 show that the

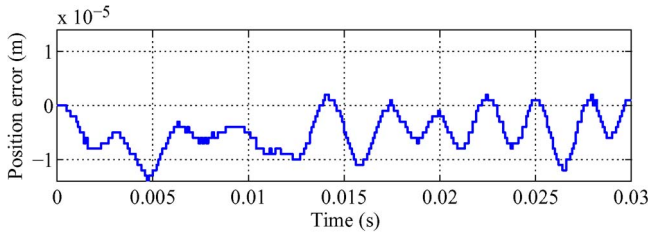

Fig. 11. Position error during motion profile, as shown in Fig. 1.

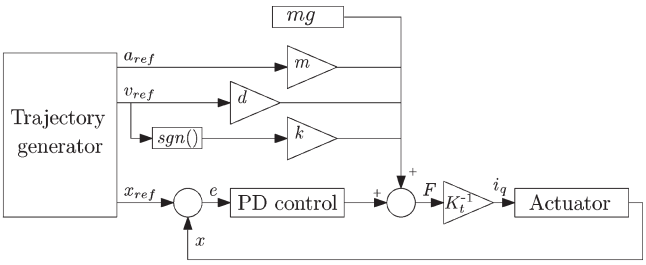

Fig. 12. Controller structure used to drive the actuator where d is the viscous friction, k is the Coulomb friction, and m is the translator mass.

peak values and the waveform show a similar behavior. However, there is a significant error between the measurements and the model. Several changes in the model are made to account for the mechanical inaccuracies in identifying the difference between the measurements and the model, but no definite agreement was found. Although the relative error between the modeled and measured values in Fig. 10 is significant, the absolute error between the model and the measurements of Figs. 8 and 10 are of the same order. Hence, the error is probably caused by other effects.

For a translator with an infinite number of magnets, the end-effect cogging force caused by the permanent magnets of the translator is periodic with the pole pitch. When the translator is moved by one pole pitch, the same geometric situation occurs. However, when the translator has a finite length, this periodicity is disturbed if one translator end is in the range of one side of the stator back iron. This effect can be seen in Figs. 8 and 10, where the center position of the translator is 15.0 mm, as also shown in Fig. 9; hence, the force profiles are symmetric around 15.0 mm. As can be seen in Fig. 10, for the minimized end-effect force, the force due to the finite length of the translator is still apparent and dominant in the force profile.

VII. Performance

To obtain the actuator performance, a controller is implemented in a Simulink dSpace environment and coupled to a three-phase current amplifier with a 3-dB bandwidth of 6 kHz. A linear optical encoder with an accuracy of 1μm is used to obtain the position. A trajectory for a stroke of 30 mm and a peak acceleration of 20 g is generated, as shown in Fig. 1. Using a feedforward and PD controller, the position error, as shown in Fig. 11, is obtained. The structure of the controller is depicted in Fig. 12. The feedforward controller contains the end-effect, acceleration, friction, and gravity compensations, and the PD controller has a sensitivity bandwidth of 250 Hz. As can be seen, the error during the trajectory is smaller than 15 μm while the final error at the end of the trajectory is only 1 μm.

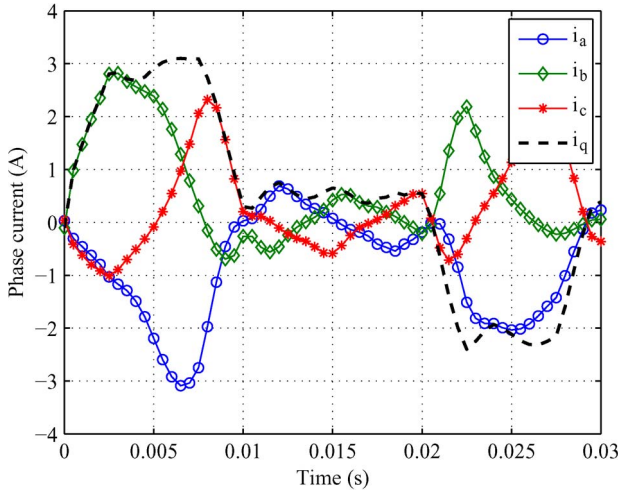

Fig. 13. Three-phase currents during motion profile shown in Fig. 1.

During the trajectory, the current setpoints for the amplifier are obtained, as shown in Fig. 13. The commutation uses the current on the q-axis to drive the actuator. This current setpoint is depicted by the dashed line in Fig. 13 while the resulting phase currents are shown by the line with the markers.

The profile of the acceleration in Fig. 1 is directly visible by i_q in Fig. 13. The jerk is clearly recognizable as the slope of the current in the initial phase. The current increases up to almost 3 A followed by an oscillation of the current originated by the end effects of the actuator. Between $t = 10$ ms and $t = 20$ ms, the current is oscillating around a value of approximately 0.5 A. As in this phase, the acceleration of the translator is zero, i.e., the translator moves at a constant speed, and the current is required to overcome the friction and gravity as the movement is upwards. The whole current waveform is symmetric around 0.5 A, and hence, in the deceleration phase, less current is required to have a zero velocity at $t = 30$ ms. Due to the friction and the gravity, the deceleration phase of an upward movement requires less power.

VIII. Thermal Analysis

From the current waveforms shown in Fig. 13 and the measured resistance of the windings, the total power dissipation is calculated. The resistance is measured at 20 °C; however, the actuator is designed for an operating temperature of $\Delta T = 40$ °C. Therefore, the measured resistance is compensated using

$$R = R_{20}(1 + \alpha \Delta T) \tag{8}$$

where α is the temperature coefficient of the resistance; for copper, $\alpha = 0.004K^{-1}$. Using this value for the resistance, the mean power during one stroke is 25.2 W. As the duty cycle is 30%, the mean power during the operation is 7.5 W. The additional heat due to the iron losses is not taken into account because the copper losses are the dominant loss component, as mentioned earlier. Due to the slit in the back iron, the eddy currents are even smaller than those calculated earlier.

The actuator is assembled to an aluminum frame to prevent vibrations. As aluminum is a very good heat conductor, this frame will act as a heat sink for the actuator. Therefore, the

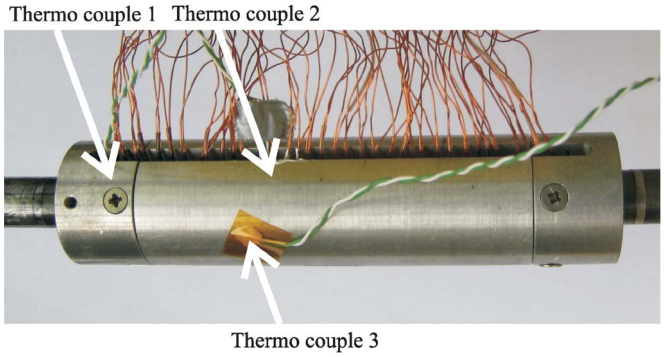

Fig. 14. Photograph of the setup with three thermocouples for thermal measurements.

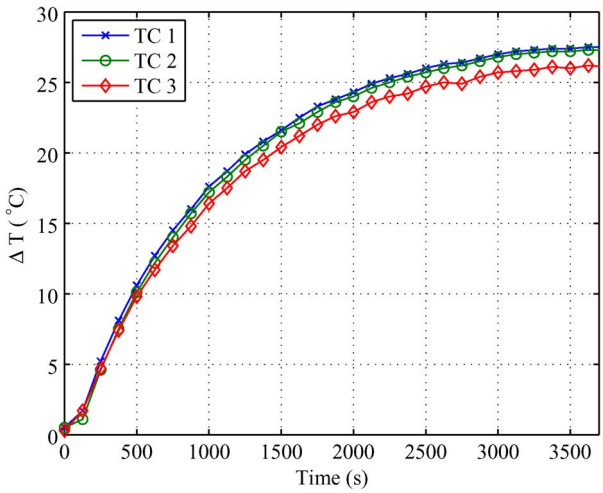

Fig. 15. Temperature measured by the three thermocouples shown in Fig. 14 while dissipating 7.5 W in the coils.

actuator is separated from the frame to enable static thermal measurements. As shown in Fig. 14, three thermocouples are placed at the actuator, two between the coils (T1 and T2) and one on the outer surface of the actuator (T3). A current is applied to the windings, and the voltage over the windings is measured. During the measurement, the value of the current is varied to dissipate a constant power of 7.5 W in the coils. The measured temperature of the three thermocouples is shown in Fig. 15; as can be seen, the temperature difference between the coils and the outer surface is approximately 2 °C. The ΔT temperature difference between the environment and the actuator is approximately 27 °C. This value is lower than the value used in the design procedure which is caused by the increased outer surface of the actuator due to the aluminum tube around the actuator. The surface of the actuator is 6.89 cm^2 while the effective surface of this prototype is 11.50 cm^2. Using

$$\Delta T = \frac{P_{\text{Cu}}}{Sh} \tag{9}$$

where S is the outer surface of the actuator, the convection coefficient h of the laboratory environment is found to be approximately 25 $\text{Wm}^{-2}\text{K}^{-1}$ without active cooling. This is higher than that considered during the design in Section III and is partly caused by the effective cooling surface. The model considers only the back iron as surface for the convection while the translator will also transfer some heat to the environment. If the aluminum tube is removed from the setup and the same convection coefficient is taken into account, the value of ΔT is approximately 44 °C which is 10% higher than the modeled value. This is mainly caused by the higher copper losses during the motion profile shown in Fig. 1 due to the decreased remanent flux density of the magnet and the friction which are not taken into account in the model. These two issues result in a decreased performance; hence, more current is required to be able to follow the trajectory resulting in a higher copper loss than that calculated in the design.

IX. Conclusion

A tubular actuator has been designed using analytical models and was built to validate the models. The actuator has been optimized to obtain the highest translator acceleration. Several static and dynamic measurements have been conducted and presented in this paper. The results show good agreement with the models used for the design. To minimize the disturbance forces, the back iron is adapted. The required acceleration has been achieved within a dynamic position accuracy of 15 μm. The thermal measurements are performed to check the feasibility of the translator acceleration with a duty cycle of 30%. Due to a lower realized remanent flux density of the magnets and an increased friction force, the temperature of the actuator is 10% higher, i.e., 44 °C instead of 40 °C, than what is expected from the models.

References

[1] N. Bianchi, S. Bolognani, D. Corte, and F. Tonel, "Tubular linear permanent magnet motors: An overall comparison," in *Conf. Rec. 37th IEEE IAS Annu. Meeting*, 2002, vol. 2, pp. 1266–1273.

[2] J. Wang, G. W. Jewell, and D. Howe, "A general framework for the analysis and design of tubular linear permanent magnet machines," *IEEE Trans. Magn.*, vol. 35, no. 3, pp. 1986–2000, May 1999.

[3] B. Gysen, E. Lomonova, J. Paulides, and A. Vandenput, "Analytical and numerical techniques for solving Laplace and Poisson equations in a tubular permanent-magnet actuator: Part I. Semi-analytical framework," *IEEE Trans. Magn.*, vol. 44, no. 7, pp. 1751–1760, Jul. 2008.

[4] S. M. Jang, J. Y. Choi, S. H. Lee, S. K. Cho, and W. B. Jang, "Analysis of the tubular motor with Halbach and radial magnet array," in *Proc. Int. Conf. Elect. Mach. Syst.*, 2003, vol. 1, pp. 250–252.

[5] J. Wang, G. Jewell, and D. Howe, "Design optimisation and comparison of tubular permanent magnet machine topologies," *Proc. Inst. Elect. Eng.—Elect. Power Appl.*, vol. 148, no. 5, pp. 456–464, Sep. 2001.

[6] L. Encica, J. J. H. Paulides, E. A. Lomonova, and A. J. A. Vandenput, "Electromagnetic and thermal design of a linear actuator using output polynomial mapping," in *Conf. Rec. 41st IEEE IAS Annu. Meeting*, Oct. 2006, vol. 4, pp. 1919–1926.

[7] J. R. Hendershot and T. J. E. Miller, *Design Of Brushless Permanent-Magnet Motors*. Labeno, OH: Magna Phys., 1994.

[8] Z. Q. Zhu, Z. P. Xia, D. Howe, and P. H. Mellor, "Reduction of cogging force in slotless linear permanent magnet motors," *Proc. Inst. Elect. Eng.—Elect. Power Appl.*, vol. 144, no. 4, pp. 277–283, Jul. 1997.

Koen J. Meessen (S'07) received the B.Sc. and M.Sc. degrees from the Department of Electrical Engineering, Eindhoven University of Technology, Eindhoven, The Netherlands, in 2008. He his currently working toward the Ph.D. degree in two-degree-of-freedom permanent-magnet actuators for pick-and-place machines at Eindhoven University of Technology.

His current research interests include the analysis, as well as the design, of high-performance electromagnetic permanent-magnet actuators.

Johannes J. H. Paulides (M'06) was born in Waalwijk, The Netherlands, in 1976. He received the B.Eng. degree from the Avans University of Applied Sciences, The Netherlands, in 1998, and the M.Phil. and Ph.D. degrees in electronic and electrical engineering from the University of Sheffield, U.K., in 2000 and 2005, respectively.

From 2005 to 2009, he was a Research Associate at Eindhoven University of Technology. Currently, he is a part-time Assistant Professor within the electromechanics and power electronics group working on more-electrical sustainable society drive systems. Since 1996 and 2008, respectively, he has been a Director of Paulides BV and Advanced Electromagnetics BV, small- and medium-sized enterprises based in The Netherlands. His research activities span all facets of electrical drives, in particular, permanent-magnet excited machines for "more electric" applications.

Dr. Paulides is a Technical and Program Committee member of the IEEE International Magnetics (INTERMAG) Conference, for which he is an Editor of the IEEE TRANSACTIONS OF MAGNETICS (conference edition).

Elena A. Lomonova (M'04–SM'07) received the M.Sc. (*cum laude*) and Ph.D. (*cum laude*) degrees in electromechanical engineering from Moscow State Aviation Institute, Moscow, Russia, in 1982 and 1993, respectively.

From 2001 to 2008, she was an Assistant Professor and then Associate Professor at Eindhoven University of Technology, Eindhoven, The Netherlands, where she became a Full-time Professor and the Chairman of the Electromechanics and Power Electronics Group in 2009. She has worked on electromechanical actuators design, optimization, and development of advanced high-precision mechatronics systems. She teaches several courses on electrical machines, advanced actuator design, finite-element method for electromechanical devices, electric components, electromechanics, electrical energy, and system integration technique. She has more than 100 published conference and peer-reviewed journal papers.